Edinburgh Research Explorer

Skeletal Mineralization Deficits and Impaired Biogenesis and Function of Chondrocyte-Derived Matrix Vesicles in Phospho1(-/-) and Phospho1/Pit1 Double Knockout Mice

Citation for published version:
Yadav, MC, Bottini, M, Cory, E, Bhattacharya, K, Kuss, P, Narisawa, S, Sah, RL, Beck, L, Fadeel, B, Farquharson, C & Millán, JL 2016, 'Skeletal Mineralization Deficits and Impaired Biogenesis and Function of Chondrocyte-Derived Matrix Vesicles in Phospho1(-/-) and Phospho1/Pit1 Double Knockout Mice' Journal of Bone and Mineral Research, vol. 31, no. 6, pp. 1275-1286. DOI: 10.1002/jbmr.2790

Digital Object Identifier (DOI):
10.1002/jbmr.2790

Link:
Link to publication record in Edinburgh Research Explorer

Document Version:
Peer reviewed version

Published In:
Journal of Bone and Mineral Research

General rights
Copyright for the publications made accessible via the Edinburgh Research Explorer is retained by the author(s) and / or other copyright owners and it is a condition of accessing these publications that users recognise and abide by the legal requirements associated with these rights.

Take down policy
The University of Edinburgh has made every reasonable effort to ensure that Edinburgh Research Explorer content complies with UK legislation. If you believe that the public display of this file breaches copyright please contact openaccess@ed.ac.uk providing details, and we will remove access to the work immediately and investigate your claim.

Download date: 05. Apr. 2019

Matrix vesicle-mediated initiation of skeletal mineralization depends on PHOSPHO1 and P_iT-1 function

Manisha C. Yadav[1], Massimo Bottini[1], Pia Kuss[1], Esther Cory[2], Robert L. Sah[2], Laurent Beck[3], Colin Farquharson[4] and José Luis Millán[1]

[1]Sanford Children's Health Research Center, Sanford-Burnham Medical Research Institute, La Jolla, CA, USA. [2]Department of Bioengineering, University of California San Diego, La Jolla, CA, USA. [3]INSERM U791, Centre for Osteoarticular and Dental Tissue Engineering (LIOAD), Nantes, Cedex, France. [4]The Roslin Institute, The University of Edinburgh, Easter Bush, Roslin, Midlothian, EH25 9RG, Scotland, UK

Running title: MV-mediated initiation of mineralization

Corresponding author:
José Luis Millán, Ph. D.
Professor
Sanford-Burnham Medical Research Institute
10901 North Torrey Pines Road
La Jolla, CA 92037
Tel: 858-646-3130
Email: millan@sanfordburnham.org

Word count:

Conflict of interest: All authors report no conflicts of interest.

ABSTRACT

We have previously shown that ablation of either the *Phospho1* or *Alpl* gene, encoding PHOSPHO1 and tissue-nonspecific alkaline phosphatase (TNAP) respectively, lead to hyperosteoidosis but that their chondrocyte- and osteoblast-derived matrix vesicles (MVs) are able to initiate mineralization. In contrast, the double ablation of *Phospho1* and *Alpl* completely abolishes initiation and progression of skeletal mineralization. We argued that MVs initiate mineralization by a dual mechanism: PHOSPHO1-mediated intravesicular generation of P_i and phosphate transporter-mediated influx of P_i generated perivesicularly. To test this hypothesis, we generated mice with the *col2a1*-driven cre-mediated ablation of P_it1 alone or in combination with a *Phospho1* gene deletion. $P_it1^{col2/col2}$ mice did not show any major phenotypic abnormalities, while severe skeletal deformities were observed in the [*Phospho1*$^{-/-}$; $P_it1^{col2/col2}$] double knockout mice that were more pronounced than those observed in the *Phospho1*$^{-/-}$ mice. Histological analysis of 15 day old [*Phospho1*$^{-/-}$; $P_it1^{col2/col2}$] bones showed growth plate abnormalities with a shorter hypertrophic chondrocyte zone and extensive hyperosteoidosis. The [*Phospho1*$^{-/-}$; $P_it1^{col2/col2}$] skeleton displayed significantly decreases in BV/TV%, trabecular number and bone mineral density (BMD) with increased trabecular separation for both tibia and femur compared to *Phospho1*$^{-/-}$ mice. Three-point bending analysis also showed that [*Phospho1*$^{-/-}$; $P_it1^{col2/col2}$] bones take longer deflection to break and show decreased maximum load and increased post-yield deflection suggesting the elastic nature of these bones. By atomic force microscopy (AFM) we found that approximately 70% of [*Phospho1*$^{-/-}$; $P_it1^{col2/col2}$] MVs were empty, in comparison to about 20-30 % empty MVs for the WT, *Phospho1*$^{-/-}$ and $P_it1^{col2/col2}$ MVs. We also found a significant decrease in the

number of MVs produced by both *Phospho1*$^{-/-}$ and [*Phospho1*$^{-/-}$; *P$_i$t1*$^{col2/col2}$] chondrocytes. These data proves the involvement of PiT-1 function in the initiation of skeletal mineralization and it provides compelling evidence that PHOSPHO1 mediates MV biogenesis.

INTRODUCTION

Mineralization of cartilage and bone occurs by a series of physicochemical and biochemical processes that together facilitate the deposition of hydroxyapatite in specific areas of the extracellular matrix (ECM). Tissue-nonspecific alkaline phosphatase (TNAP) plays a crucial role in restricting the concentration of the mineralization inhibitor inorganic pyrophosphate (PP_i) to maintain a P_i/PP_i ratio permissive for normal propagation of mineral in the extracellular matrix (Moss *et al*., 1967; Majeska *et al*., 1975; Johnson *et al*., 2000; Hessle *et al*., 2002; Murshed *et al*., 2005; Yadav *et al*., 2011; Millán, 2012; McKee *et al*., 2013). *Alpl*$^{-/-}$ mice chondrocyte and osteoblast-derived matrix vesicles (MVs) however are still able to initiate mineralization (Anderson et al., 1997, 2004), indicating that other enzymes or mechanisms are involved in the intravesicular initiation of mineralization. Subsequently, we showed that PHOSPHO1, an enzyme that uses phosphocholine and phosphoethanolamine to concentrate P_i inside MVs, is also required for proper bone mineralization (Roberts et al., 2007; Huesa *et al*., 2011; Yadav *et al*., 2011; McKee *et al*., 2013), as the lack of PHOSPHO1 (*Phospho1*$^{-/-}$ mice) also leads to skeletal and dental hypomineralization. Importantly, the [*Alpl*$^{-/-}$; *Phospho1*$^{-/-}$] double knockout mice are embryonic lethal and the E16.5 embryos show complete absence of skeletal mineralization and MVs devoid of mineral (Yadav et al., 2011). We hypothesized that MV-mediated initiation of mineralization results from a dual mechanism, i.e. PHOSPHO1-mediated intra-vesicular production and transporter-mediated influx of P_i. Two related type III Na/Pi co-transporters, P_iT-1/Glvr1 and P_iT-2/Ram, are both expressed by chondrocytes and osteoblasts, but literature reports that PiT-1 is the major mediator of P_i influx in these cell types (Nielsen *et al*., 2001; Yoshiko *et al.*, 2007; Polewski *et al.*, 2010). Thus, to test this hypothesis we generated mice with a conditional ablation of P_iT-1 gene (*Slc20a1*, here referred to as *Pit1*) alone or in the *Phospho1*$^{-/-}$ background. Our data proves the involvement of P_iT-1 function in the initiation of endochondral ossification and also points to PHOSPHO1 as an enzyme controlling MV biogenesis.

MATERIALS AND METHODS

Mice

Phospho1-R74X null mutant (*Phospho1*$^{-/-}$) mice were generated as described (Yadav et al., 2011). The generation and characterization of the $P_it1^{flox/flox}$ mice was reported earlier (Beck et al., 2010). To generate mice lacking both PHOSPHO1 and P$_i$T-11, *Phospho1*$^{-/-}$ mice were crossed to $P_it1^{flox/flox}$ mice and double heterozygote mice were used to generate [*Phospho1*$^{-/-}$; $P_it1^{flox/flox}$] double mutant mice. These mice were then bred with *Col2a1-cre* mice to generate [$P_it1^{flox/flox}$*; Col2a1-cre*], here named $P_it1^{col2/col2}$ and [*Phospho1*$^{-/-}$; $P_it1^{col2/col2}$] mice. *Phospho1*$^{-/-}$ genotypes were determined using genomic DNA, PCR and restriction digestion by BsrD1 restriction enzyme (Yadav et al., 2011). $P_it1^{col2/col2}$ and [*Phospho1*$^{-/-}$; $P_it1^{col2/col2}$] mice were genotyped by PCR. The primer sequences for genotyping were: *Phospho1*: F 5' TCCTCCTCACCTTCGACTTC -3', R 5'-ATGCGGCGGAATAAACTGT -3', $P_it1^{flox/flox}$: F 5' AAGGCATTTGTCAGCCCAGTC-3', R 5' ATCGATCCACTCAGTCTAGTGC-3' and *Col2a1-cre*: zndhhc14 F-5' GGCAGGAAAGAGTCCAGGTATG-3', zndhhc14 R-5' – TAAGCACTGACAGATGACCTGC-3', *Col2a1-cre* F-5' TTAGCCTGGATAGAGCAACCGC-3'.

Tissue and plasma collection and histological studies

Mice were anesthetized by intraperitoneal injection of Avertin and blood was collected by cardiac puncture. Whole-body, long bones and spine radiographic images were taken using an MX20 Specimen Radiograph System (Faxitron X-ray Corporation, Chicago, IL, USA) at 1 month of age. The lumbar spines, tibias, and femurs of 15-days-old mice were fixed in PBS containing 4% (vol/vol) paraformaldehyde. Paraffin or plastic sections were stained with Von Kossa/Van Gieson stain using standard procedures (Murshed *et al*., 2005; Millan *et al*., 2008 and Narisawa *et al*., 2001). Von Kossa/Van Gieson–stained slides were used for quantification of osteoid volume using the Bioquant Osteo Software (Bioquant Osteoanalysis Co., Nashville, TN, USA.

For P_iT-1 immunohistochemistry, bone tissues were decalcified with 0.125 M EDTA/10% formalin in H_2O (pH 7.2) for five days after fixation, and processed for paraffin sectioning. Immunostaining was performed using a standard avidin-biotin complex protocol using the Vectastatin ABC kit (Vector laboratories Inc, Burlingame, CA). Rabbit anti-mouse OPN antibody (Santa Cruz Biotechnology Inc, Santa Cruz, CA, USA) was used for detection of P_iT-1.

P_it1 gene expression

Primary chondrocytes from WT and $P_it1^{col2/col2}$ mice were isolated from the knee joint growth plates of 5 day-old pups by collagenase digestion, as described previously (Yadav et al., 2011). RNA was extracted using RNAeasy Pus Kit (Qiagen, Valencia, CA, USA). Specific RNA transcript (mRNA) for *Pit1* was quantified by real-time PCR using dual-labeled hydrolysis probes (FAM-TAMRA). P_it1 primers and probe sequences are as follows: F-5’GGCTCAGGTGTAGTGACCCT3’, R-5’ CACATCTATCAAGCCGTTCC3’ and FAM-TAMRA Probe-5’CGAAACTGTGGGCTCCGCC3’.

Biochemical assays

Blood was collected by cardiac puncture into lithium heparin tubes and plasma was collected by centrifugation at 5000 rpm for 10min. Alkaline phosphatase activity in plasma was measured using a previously reported method (Millán *et al.*, 2008). PP_i levels were measured using activated charcoal and ^3H method as we previously reported (Mcguire et al., 1980; Yadav et al, 2011). Calcium levels were measured using the cresolphthalein complexone liquicolor test kit (Stanbio, Boerne, Tx, USA) according to the manufacturer's protocol.

Micro–computed tomography (μCT)

Mice were euthanized at 1 month of age, the tibias and femurs dissected and fixed in 4% paraformaldehyde. Samples were imaged on a μCT scanner (Skyscan 1076, Kontich, Belgium). Samples were wrapped in tissue paper that was moistened with phosphate buffered saline (PBS), and scanned at 9μm voxel size, applying an electrical potential of 50 kVp and current of 200uA, using a 0.5mm aluminum filter. Mineral density was determined by calibration of images against 2mm diameter hydroxyapatite (HA) rods (0.25 and 0.75 gHA/cm3). Additionally, a beam hardening correction algorithm was applied prior to image reconstruction.

To visualize and determine bone histomorphometric parameters, the software, Dataviewer, CTAn, CTVol and CTVox (all Skyscan, Kontich, Belgium) was used. Cortical bone analysis was performed on the femur and tibia midshafts. The volumes of interest were selected in reference to an identified landmark1. Since all animals were 1 month of age, the volumes of interest were (1) 3600-4500 μm proximal to the distal femur growth plate and (2) 3600-4500 μm distal to the tibia proximal growth plate. The cortical bone in this region was selected by automatic contouring of the periosteal tissue excluding the marrow cavity. A global threshold was used to identify cortical bone and an erosion of one pixel was performed to eliminate partial volume effects. From these regions of femoral and tibial cortical bone, the following parameters were determined: cross-sectional tissue area (T.Ar), cross-sectional cortical bone area (B.Ar), cortical bone area fraction (B.Ar/T.Ar), cross-sectional bone thickness (Cs.Th) and tissue mineral density (TMD).

Trabecular bone analysis was performed at the distal femoral metaphysis and proximal tibial metaphysis. The regions of interest were (1) 360-2160 μm proximal to the distal femoral growth plate, and (2) 360-2160 μm distal to the proximal tibial growth plate. The trabecular region was selected by automatic contouring. An adaptive threshold (using the mean maximum and minimum pixel intensity values of the surrounding ten pixels) was used to identify trabecular bone and an erosion of one pixel was performed to eliminate partial volume effects. From these regions of femoral and tibial trabecular bone the following parameters were determined: tissue volume (TV), trabecular bone volume (BV), trabecular bone volume fraction (BV/TV), trabecular thickness (Tb.Th), trabecular separation (Tb.Sp), trabecular number (Tb.N), structure model index (SMI), trabecular pattern factor (Tb.Pf), and bone mineral density (BMD). μCT analyses of the trabecular bone was performed on a 2mm section of the right tibial and femoral metaphysis 250 μm distal to the growth plate using a Skyscan 1172 instrument (Kontlich, Belgium) set at 60 kV, 150 µA and at a resolution of 5 µm. The cortical analysis was conducted on a 250 µm section 2.25 mm distal of the reference growth plate. The spines were dissected from the cervical to the second lumbar vertebrae and the thoracic vertebrae scanned at a resolution of 20µm. The images were reconstructed using the Skyscan NRecon program, analyzed using Skyscan CTAn and the 3 dimensional (3D) models visualized in CTvol software (Yadav *et al*., 2011).

3-point bending for the determination of bone stiffness and breaking strength

An Instron 3342 materials testing machine (Instron, Norwood, MA, USA) fitted with a 2 kN load cell was used to determine bone stiffness and breaking strength (Aspden, 2003). The span was fixed at 5.12 mm for femurs. The cross-head was lowered at 1 mm/min and data were recorded after every 0.2 N change in load and every 0.1 mm change in deflection. Each bone was tested to fracture. Failure and fracture points were identified from the load-extension curve as the point of maximum load and where the load rapidly decreased to zero, respectively. The maximum stiffness was defined as the maximum gradient of the rising portion of this curve, and the yield point, the point at which the gradient reduced to 95% of this value. Both values were calculated from a polynomial curve fitted to the rising region of the load-extension curve in Mathcad (Mathsoft Engineering and Education Inc., Cambridge, MA, USA).

Atomic force microscopy (AFM)

A drop (5 µL) of each MV solution in Tris-buffered-saline was spotted on freshly cleaved mica substrates (Ted Pella, Redding, CA) and allowed to stand for 5 min. Next, 5 µL of glutaraldehyde solution (8% in H_2O, Sigma-Aldrich, St. Louis, MO) was dropped onto the samples. The substrates were stored inside a desiccators at room temperature for 24 h. AFM images of dried samples were recorded in air by means of an 5500 atomic force microscope (Agilent Technologies, Santa Clara, CA) equipped with an open-loop probe working in non-contact (AAC) mode. Silicon-nitride cantilevers having a nominal resonance frequency of ~190 kHz (NanosensorsTM, Neuchatel, Switzerland) were used. Tridimensional AFM images were generated by PicoView software (Agilent Technologies).

AFM images were used to gather information about the morphology and number of MVs in each sample. The cross section of N=100 MVs in each sample was recorded and the MVs' diameter was calculated as the peak value in the cross section. The number of MVs in each sample was calculated as number of MVs *per* μm^2 by counting the globular features in N=20 scan fields (2 × 2 μm). Mean and SD values were obtained through Gaussian fit of the value distributions.

Statistical analysis

All measurements were performed at least in triplicate. Results are expressed as mean ± SEM. The data were analyzed using Student's t test. P values less than 0.05 were considered significant. For AFM, statistical differences among samples were calculated by non-parametric Mann–Whitney U analysis performed by SPSS Statistics (IBM Corporation, Armonk, NY).

RESULTS

Skeletal phenotype of [*Phospho1*$^{-/-}$; *Pit1*$^{col2/col2}$] mice

Immunohistochemistry demonstrated reduced P$_i$T-1 expression in the proliferative and hypertrophic chondrocyte area of the knee joint section of the growth plate of 1-month-old *P*$_i$*t1*$^{col2/col2}$ mice compared to WT mice (Fig. 1A). There was visible residual P$_i$T1 expression in these cells that was estimated to be 35% by qPCR (Fig. 1B). The *P*$_i$*t1*$^{col2/col2}$ mice were comparable to WT mice in size but the [*Phospho1*$^{-/-}$; *P*$_i$*t1*$^{col2/col2}$] mice were even smaller than age-matched *Phospho1*$^{-/-}$ mice, which we had shown to be runted (Yadav et al., 2011) (Fig. 1C). The [*Phospho1*$^{-/-}$; *P*$_i$*t1*$^{col2/col2}$] skeletons showed exacerbated abnormalities compared to the *Phospho1*$^{-/-}$ mice, including multiple fractures and callus formation in the ribs, increased bowing of the long bones and increased prevalence of fractures in these bones (Fig. 2).

Histology evidenced shortened growth plate in the [*Phospho1*$^{-/-}$; *P*$_i$*t1*$^{col2/col2}$] bones (Fig. 3A). Histomorphometric analyses in 15-days-old mice confirmed the osteomalacia previously reported in 10-days-old and 1-month-old *Phospho1*$^{-/-}$ mice (Yadav et al., 2011, 2014) (Fig. 3A, arrows), and showed worsening of this phenotype in the tibias of [*Phospho1*$^{-/-}$; *P*$_i$*t1*$^{col2/col2}$] mice (BV/TV%, WT = 43.16 ± 2.924, *Phospho1*$^{-/-}$ = 24.87 ± 1.055, *P*$_i$*t1*$^{col2/col2}$ = 40.04 ± 3.23, [*Phospho1*$^{-/-}$; *P*$_i$*t1*$^{col2/col2}$] =17.85 ± 1.51, n=3; WT vs [*Phospho1*$^{-/-}$; *P*$_i$*t1*$^{col2/col2}$], p=0.002; *Phospho1*$^{-/-}$ vs [*Phospho1*$^{-/-}$; *P*$_i$*t1*$^{col2/col2}$], p=0.02; *P*$_i$*t1*$^{col2/col2}$ vs [*Phospho1*$^{-/-}$; *P*$_i$*t1*$^{col2/col2}$], p=0.003; WT vs [*Phospho1*$^{-/-}$; *P*$_i$*t1*$^{col2/col2}$], p=0.5) and (OV/BV%, WT= 0.0017 ± 9.405e-005, *Phospho1*$^{-/-}$ = 9.87 ± 3.18, *P*$_i$*t1*$^{col2/col2}$ = 0.0018 ± 0.00010, [*Phospho1*$^{-/-}$; *P*$_i$*t1*$^{col2/col2}$] =24.80 ± 1.82, n=3; WT vs [*Phospho1*$^{-/-}$;

$P_it1^{col2/col2}$], p=0.0002; *Phospho1*$^{-/-}$ vs [*Phospho1*$^{-/-}$; $P_it1^{col2/col2}$], p=0.04; $P_it1^{col2/col2}$ vs [*Phospho1*$^{-/-}$; $P_it1^{col2/col2}$], p=0.0002; WT vs [*Phospho1*$^{-/-}$; $P_it1^{col2/col2}$], p=0.75) (Fig. 2A). There was a complete absence of mineralization in the trabecular bone in certain areas (arrows). The secondary ossification centers also show increased amount of osteoid in these mice. The vertebral sections also showed the presence of widespread hyperosteoidosis in the *Phospho1*$^{-/-}$ mice (Fig. 3B, arrows), which further increased in [*Phospho1*$^{-/-}$; $P_it1^{col2/col2}$] mice (BV/TV%, WT= 33.22 ± 2.01, *Phospho1*$^{-/-}$ = 24.08 ± 1.35, $P_it1^{col2/col2}$ =31.96±0.61, [*Phospho1*$^{-/-}$; $P_it1^{col2/col2}$] =18.87±0.64, n=3; WT vs [*Phospho1*$^{-/-}$; $P_it1^{col2/col2}$], p=0.002; *Phospho1*$^{-/-}$ vs [*Phospho1*$^{-/-}$; $P_it1^{col2/col2}$], p=0.02; $P_it1^{col2/col2}$ vs [*Phospho1*$^{-/-}$; $P_it1^{col2/col2}$], p=0.0001; WT vs [*Phospho1*$^{-/-}$; $P_it1^{col2/col2}$], p=0.58) and (OV/BV%, WT= 0.0028 ± 0.00017, *Phospho1*$^{-/-}$ = 3.96 ± 1.16, $P_it1^{col2/col2}$ = 0.0027 ± 0.00011, [*Phospho1*$^{-/-}$; $P_it1^{col2/col2}$] =9.82 ± 0.99, n=3; WT vs [*Phospho1*$^{-/-}$; $P_it1^{col2/col2}$], p=0.0006; *Phospho1*$^{-/-}$ vs [*Phospho1*$^{-/-}$; $P_it1^{col2/col2}$], p=0.02; $P_it1^{col2/col2}$ vs [*Phospho1*$^{-/-}$; $P_it1^{col2/col2}$], p=0.0006; WT vs [*Phospho1*$^{-/-}$; $P_it1^{col2/col2}$], p=0.68) (Fig. 3B).

μCT analysis concurred with the radiographic and histology data showing enhanced bowing of the long bones in both tibia and femur of the [*Phospho1*$^{-/-}$; $P_it1^{col2/col2}$] compared to the *Phospho1*$^{-/-}$ mice (Fig. 4A, B). Trabecular parameters of the femur (Table 1) of [*Phospho1*$^{-/-}$; $P_it1^{col2/col2}$] compared to *Phospho1*$^{-/-}$ mice showed significantly decreased BV/TV% (p=0.003), increased trabecular separation (p= 0.02), decreased trabecular number p=0.002) and decreased bone mineral density (p=0.002). Similarly for the tibia (Table 2) the [*Phospho1*$^{-/-}$; $P_it1^{col2/col2}$] compared to *Phospho1*$^{-/-}$ mice showed significantly decreased BV/TV% (p=0.003) increased trabecular separation (p= 0.002), decreased trabecular number (p=0.001) and decreased bone mineral density (p=0.01). Also, the cortical parameters of femur (Table 3) show significantly decreased relative bone area (p= 0.01) and cross-sectional area (p= 0.01) in the [*Phospho1*$^{-/-}$; *P$_i$t1*$^{col2/col2}$] compared to *Phospho1*$^{-/-}$ mice. Similarly, the cortical parameters of femur in these mice show significantly decreased relative bone area (p= 0.02), cross-sectional area (p= 0.02) and also the tissue mineral density (p=0.03). The *P$_i$t1*$^{col2/col2}$ mice also show reduced BV/TV%, trabecular number and thickness and increased trabecular separations in the femur as compared to the WT mice. Similar results were observed for the tibia (Table 4). Three-point bending analysis demonstrated that *P$_i$t1*$^{col2/col2}$ femurs break like WT but take a little longer deflection to break as compared to the WT mice. However, [*Phospho1*$^{-/-}$; *P$_i$t1*$^{col2/col2}$] bones take even longer deflection and do not break (Fig. 5).

Reduced plasma TNAP activity was observed in 1-month-old [*Phospho1*$^{-/-}$; *P$_i$t1*$^{col2/col2}$] mice compared to WT mice (Fig. 6A). Consistent with the measured TNAP levels we measured increased plasma PP$_i$ levels in [*Phospho1*$^{-/-}$; *P$_i$t1*$^{col2/col2}$] compared to WT, *P$_i$t1*$^{col2/col2}$ and *Phospho1*$^{-/-}$ mice (Fig. 6B).

Analyses of MVs

We used atomic force microscopy (AFM) to investigate the morphology (shape and diameter) and numbers of isolated MVs. MVs appeared spherical and either individually dispersed or connected to ~1 nm-thick chains, which were interpreted as cytoskeleton macromolecules (Supplemental Fig. 1). Air-dried MVs were imaged without any coating or first coated with glutaraldehyde and then dried before imaging to calculate the number of filled vs unfilled MV (Supplemental Fig. 2A, B). The distribution of the height of the vesicles was different among samples. WT MVs showed a bi-modal distribution of height values with a narrow peak centered at ~ 2.3 nm and a broad one centered at ~7.4 nm, respectively (Supplemental Fig. 2C). Similar bi-modal distribution of height values was found for $P_it1^{col2/col2}$ MVs. *Phospho1*$^{-/-}$ MVs and [*Phospho1*$^{-/-}$; $P_it1^{col2/col2}$] MVs also show a bimodal distribution but with much smaller values. For *Phospho1*$^{-/-}$ the broad peak was at 4.8 nm and the narrow peak was at 1.8nm. The [*Phospho1*$^{-/-}$; $P_it1^{col2/col2}$] mice show even smaller heights as compared to *Phospho1*$^{-/-}$, as the broad peak was at 3.9 nm and the narrow peak was at 1.9 nm. We interpreted the MVs with a height lower than 7 nm as unfilled MVs, whereas those with a height greater than 7 nm as filled MVs. Thus, we found that WT and $P_it1^{col2/col2}$ MVs were mostly filled (xx% and xx% of filled MVs, respectively), whereas *Phospho1*$^{-/-}$ MVs and [*Phospho1*$^{-/-}$; $P_it1^{col2/col2}$] MVs were mostly unfilled (xx% and xx% of filled MVs, respectively) (Fig. 7A). Additionally, we found that empty MVs in the [*Phospho1*$^{-/-}$; $P_it1^{col2/col2}$] preparations were smaller than those in the *Phospho1*$^{-/-}$ samples. We also determined the volume of these MVs (Supplemental Fig. 2D) and observed that WT and $P_it1^{col2/col2}$ MVs have broader volume peaks corresponding to 143 x 10^3 nm^3 and 135 x10^3 nm^3. However, the *Phospho1*$^{-/-}$ MVs had a volume peak at 35 x 10^3 nm^3 and the [*Phospho1*$^{-/-}$; $P_it1^{col2/col2}$] MVs had even lesser volume of 16 x 10^3 nm^3, in agreement with our interpretation based on the height data that these vesicles were mostly unfilled. Finally, we found that the number of MVs *per* µm^2 for the *Phospho1*$^{-/-}$ and [*Phospho1*$^{-/-}$; $P_it1^{col2/col2}$] samples was significantly lower than the number of MVs in the WT and $P_it1^{col2/col2}$ samples (Fig. 7B). The slight difference in number of MVs *per* µm^2 was not statistically significant. These data clearly point to a role of PHOSPHO1 in MV biogenesis.

DISCUSSION

Table 1: Trabecular parameter of the femur.

Sample	**Site**	**Tissue Volume TV mm^3**	**Bone Volume BV mm^3**	**Relative Bone Volume BV/TV %**	**Trabecular Thickness Tb.Th mm**	**Trabecular Separation Tb.Sp mm**	**Trabecular Number Tb.N 1/mm**	**Structure Model Index SMI**	**Trabecular pattern factor Tb.Pf 1/mm**	**Bone Mineral Density BMD g/cm^3**
WT	Femur	1.80	0.17	9.33	0.04	0.21	2.36	1.97	27.17	0.22
Phospho1$^{-/-}$	Femur	*2.17*	*0.14*	*6.50*	*0.03*	*0.21*	*1.87*	*2.13*	*33.75*	*0.17*
P$_{i}$***t1*** $^{flox/flox}$***; Col2a1-cre***	Femur	2.57	0.15	5.74	0.03	0.24	1.72	2.18	35.76	0.14
Phospho1$^{-/-}$***; P***$_{i}$***t1*** $^{flox/flox}$***; Col2a1-cre***	Femur	1.56	0.05	3.11	0.03	0.30	0.93	2.44	43.81	0.10

Table 2: Trabecular parameters of the tibia

Sample	**Site**	**Tissue Volume TV mm^3**	**Bone Volume BV mm^3**	**Relative Bone Volume BV/TV %**	**Trabecular Thickness Tb.Th mm**	**Trabecular Separation Tb.Sp mm**	**Trabecular Number Tb.N 1/mm**	**Structure Model Index SMI**	**Trabecular pattern factor Tb.Pf 1/mm**	**Bone Mineral Density BMD g/cm^3**
WT	Tibia	1.10	0.05	4.57	0.03	0.23	1.53	2.18	39.37	0.17
Phospho1$^{-/-}$	Tibia	1.64	0.07	4.49	0.03	0.22	1.56	2.15	39.63	0.16
P$_{i}$***t1*** $^{flox/flox}$***; Col2a1-cre***	Tibia	1.87	0.07	3.52	0.03	0.26	1.24	2.23	41.52	0.12
Phospho1$^{-/-}$***; P***$_{i}$***t1*** $^{flox/flox}$***; Col2a1-cre***	Tibia	1.09	0.04	3.30	0.03	0.26	1.10	2.34	43.31	0.11

Table 3: Cortical parameters of the femur

		Cross-sectional Tissue Area	**Cross-sectional Bone Area**	**Relative Bone Area**	**Cross-sectional thickness**	**Tissue Mineral Density**
		T.Ar	**B.Ar**	**B.Ar/T.Ar**	**Cs.Th**	**TMD**
Sample	**Site**	**mm^2**	**mm^2**	**%**	**mm**	**g/cm3**
WT	Femur	1.500	0.654	42.95	0.160	0.892
Phospho1$^{-/-}$	Femur	1.824	0.732	40.19	0.147	0.866
P_i***t1*** $^{flox/flox}$***; Col2a1-cre***	Femur	1.668	0.651	38.97	0.140	0.904
Phospho1$^{-/-}$***;*** P_i***t1*** $^{flox/flox}$***; Col2a1-cre***	Femur	1.533	0.478	30.846	0.107	0.846

Table 4: Cortical parameters of the tibia

Sample	Site	Cross-sectional Tissue Area T.Ar mm^2	Cross-sectional Bone Area B.Ar mm^2	Relative Bone Area B.Ar/T.Ar %	Cross-sectional thickness Cs.Th mm	Tissue Mineral Density TMD g/cm3
WT	Tibia	1.496	0.643	42.04	0.158	1.005
Phospho1 $^{-/-}$	Tibia	1.609	0.670	41.60	0.150	0.919
$P_it1^{flox/flox}$***; Col2a1-cre***	Tibia	1.700	0.610	35.82	0.125	0.927
Phospho1 $^{-/-}$; $P_it1^{flox/flox}$***; Col2a1-cre***	Tibia	1.447	0.507	34.666	0.119	0.867

LEGEND TO FIGURES

Fig.1: Phenotypic abnormalities in [*Phospho1*$^{-/-}$; *P*$_i$*t1*$^{col2/col2}$] mice. (A) Immunohistochemistry using anti-P$_i$T1 antibody on the femur from *Phospho1*$^{-/-}$ and *P*$_i$*t1*$^{col2/col2}$ mice shows reduced P$_i$T-1 expression in the hypertrophic chondrocyte region of *P*$_i$*t1*$^{col2/col2}$ mice. B) qRT-PCR showing visible residual *P*$_i$*t1* gene expression (~35%) in chondrocytes (C) *Phospho1*$^{-/-}$ mice are smaller than WT mice and the [*Phospho1*$^{-/-}$; *P*$_i$*t1*$^{col2/col2}$] mice were even smaller than the *Phospho1*$^{-/-}$ mice.

Fig. 2: X-ray images. Radiographic images showed worsening of the skeletal abnormalities (arrows) in [*Phospho1*$^{-/-}$; *P*$_i$*t1*$^{col2/col2}$] mice as compared to the *Phospho1*$^{-/-}$ mice. Arrows show highly bowed long bones and multiple fractures in the spine and limbs in [*Phospho1*$^{-/-}$; *P*$_i$*t1*$^{col2/col2}$] mice.

Fig. 3: Histomorphometric analyses of tibias (A) and spines (B) of *Phospho1*$^{-/-}$ and [*Phospho1*$^{-/-}$; *P*$_i$*t1*$^{col2/col2}$] mice at 15-days of age. Images for WT and *P*$_i$*t1*$^{col2/col2}$ not shown. Histograms show comparison between WT, *Phospho1*$^{-/-}$, *P*$_i$*t1*$^{col2/col2}$ and [*Phospho1*$^{-/-}$; *P*$_i$*t1*$^{col2/col2}$] mice for BV/TV% and OV/BV% for tibia (A) and spine (B). Von Kossa/van Gieson staining of the tibial section at the knee joint reveals trabecular bone surrounded by widespread, extended osteoid in 15-day-old *Phospho1*$^{-/-}$ mice (arrows the areas where the osteoid is present) as compared to the WT mice. The *P*$_i$*t1*$^{col2/col2}$ mice appear similar to the WT mice with no osteoid. However, the [*Phospho1*$^{-/-}$; *P*$_i$*t1*$^{col2/col2}$] mice show even more unmineralized bone in tibia (trabecular bone, secondary

ossification center) as well as in the spine (vertebrae).

Fig. 4: μCT analysis of femur and tibia in WT, *Phospho1*$^{-/-}$, *P*$_i$*t1*$^{col2/col2}$ and [*Phospho1*$^{-/-}$; *P*$_i$*t1*$^{col2/col2}$] mice at 1 month of age. (A) 3D volume renders of the full samples (side view –full leg, front view-tibia, anterior view-femur) 2D orthogonal cross-sections of femurs and tibiae. Both 2d volume renders and 3d orthogonal cross-sections show highly bowed/ twisted long bones in [*Phospho1*$^{-/-}$; *P*$_i$*t1*$^{col2/col2}$] mice compared to WT, *P*$_i$*t1*$^{col2/col2}$ and even *Phospho1*$^{-/-}$ mice.

Fig. 5: Three-point bending load vs extension graphs on WT (n=6) (A), *Phospho1*$^{-/-}$ (n=4) (B), *P*$_i$*t1*$^{col2/col2}$ (n=7) (C) and [*Phospho1*$^{-/-}$; *P*$_i$*t1*$^{col2/col2}$] (n=5) (D) mice femurs. *P*$_i$*t1*$^{col2/col2}$ mice show similar break pattern to the WT mice. In contrast, *Phospho1*$^{-/-}$ mice femurs take longer deflection to break and the [*Phospho1*$^{-/-}$; *P*$_i$*t1*$^{col2/col2}$] femurs take even longer to break.

Fig. 6: Plasma levels of TNAP and PP_i. (A) TNAP activity (B) and PP_i concentration in plasma of 1-month-old mice. TNAP levels were lower and PP_i levels were higher in the plasma of *P*$_i$*t1*$^{col2/col2}$ and [*Phospho1*$^{-/-}$; *P*$_i$*t1*$^{col2/col2}$] mice than in WT and *Phospho1*$^{-/-}$ mice. Data are represented as mean ± SEM, n= 6 mice per group, experiments performed in duplicate.

Fig. 7. Determination of percentage of filled MVs and total number of MVs. A) We observed a statistically significant decrease in the number of filled MVs in the [*Phospho1*$^{-/-}$; *P*$_i$*t1*$^{col2/col2}$] samples compared to WT, *Phospho1*$^{-/-}$ and *P*$_i$*t1*$^{col2/col2}$ samples.

B) The *Phospho1*$^{-/-}$ MV preparations show a statistically significant decrease in the total number of MVs. The [*Phospho1*$^{-/-}$; *P*$_{i}$*t1*$^{col2/col2}$] MV preparations show a comparable decrease in the number of MVs.

Supplemental Fig. 1: MVs were found in chains (A, B) and considered as spheroids with the polar diameter (a) as the MV height and the polar diameter (b) as the MV's width at half height (C).

Supplemental Fig. 2: Atomic force microscopy (AFM) of filled (A) and unfilled (B) MVs. From left to right: topography, amplitude and three-dimensional reconstruction. AFM images were recorded in non-contact (AAC) mode. Height (C) and volume (D) distribution for isolated MVs from WT, *Phospho1*$^{-/-}$, *P*$_{i}$*t1*$^{flox/flox}$; *Col2a1-cre* and [*Phospho1*$^{-/-}$; *P*$_{i}$*t1*$^{flox/flox}$; *Col2a1-cre*] mice. Peaks were fitted by Gaussian curves. MVs' volumes have been calculated by assuming MVs as spheroidal structures.

REFERENCES

Anderson HC, Garimella R, Tague SE 2005 The role of matrix vesicles in growth plate development and biomineralization. Front Biosci 10:822–837.

Anderson HC, Hsu HHT, Morris DC, Fedde KN, Whyte MP. Matrix vesicles in osteomalacic hypophosphatasia bone contain apatite-like mineral crystals. Am J Pathol. 1997;151:1555–1561.

Anderson HC, Sipe JE, Hessle L, et al. Impaired calcification around matrix vesicles of growth plate and bone in alkaline phosphatase deficient mice. Am J Pathol. 2004;164:841–847.

Aspden RM. Mechanical testing of bone ex vivo. Methods Mol Med. 2003; 80:369–379.

Caverzasio J, Bonjour JP 1996 Characteristics and regulation of Pi transport in osteogenic cells for bone metabolism. Kidney Int 49:975–980.

Caverzasio J, Montessuit C, Bonjour JP 1996 Functional role of Pi transport in osteogenic cells. News Physiol Sci 11:119–125.

Caverzasio J, Murer H, Tenenhouse HS 2003 Phosphate Homeostasis, Regulatory Mechanisms. Pediatric Bone. Biology & Diseases. Elsevier Science, San Diego, CA, USA.

Cecil DL, Rose DM, Terkeltaub R, Liu-Bryan R 2005 Role of interleukin-8 in PiT-1 expression and CXCR1-mediated inorganic phosphate uptake in chondrocytes. Arthritis Rheum 52:144–154.

Fedde KN, Blair L, Silverstein J, et al. Alkaline phosphatase knock-out mice recapitulate the metabolic and skeletal defects of infantile hypophosphatasia. J Bone Miner Res. 1999;14:2015–2026.

Giachelli CM, Speer MY, Li X, Rajachar RM, Yang H 2005 Regulation of vascular calcification: Roles of phosphate and osteopontin. Circ Res 96:717–722.

Hessle L, Johnson KA, Anderson HC, et al. Tissue-nonspecific alkaline phosphatase and plasma cell membrane glycoprotein-1 are central antagonistic regulators of bone mineralization. Proc Natl Acad Sci USA. 2002;99:9445–9449.

Huesa C, Yadav MC, Finnila MAJ, Goodyear SR, Robins SP, Tanner KR, Aspden RM, Millán, JL, Farquharson C. PHOSPHO1 is essential for mechanically competent mineralization and the avoidance of spontaneous fractures. Bone. 2011;48:1066-1077.

Johnson KA, Hessle L, Vaingankar S, et al. Osteoblast tissue-nonspecific alkaline phosphatase antagonizes and regulates PC-1. Am J Physiol Regul Integr Comp Physiol.

2000;279:R1365–1377.

Kuzynski, M., Goss, M., Bottini, M., Yadav, M.C., Mobley, C., Winters, T., Poliard, A., Kellermann, O., Lee, B., Millan, J. L., and Napierala, D. Dual role of the Trps1 transcription factor in dentin mineralization. J Biol Chem. 2014 Oct 3;289(40):27481-93.

Loghman-Adham M, Szczepanska-Konkel M, Yusufi AN, Van Scoy M, Dousa TP 1987 Inhibition of Na+-Pi cotransporter in small gut brush border by phosphonocarboxylic acids. Am J Physiol 252:G244–G249.

Majeska RJ, Wuthier RE. Studies on matrix vesicles isolated from chick epiphyseal cartilage. Association of pyrophosphatase and ATPase activities with alkaline phosphatase. Biochem Biophys Acta. 1975; 391:51–50.

McGuire, M B, Olman, CH, Baghat, N. and Russell, RG. Radiometric measurement of pyrophosphate in cell cultures. Biochem. Soc. Trans. 1980;8:529-530.

McKee MD, Yadav MC, Foster BL, Somerman MJ, Farquharson C, Millán, JL. Compounded PHOSPHO1/ALPL Deficiencies Reduce Dentin Mineralization. J Dent Res. 2013;92:721-727.

Millán J.L. The Role of Phosphatases in the Initiation of Skeletal Mineralization. Calcif Tissue Int. 2012:ePub ahead of print. Epub 2012/11/28. doi: 10.1007/s00223-012-9672-8.

Moss DW, Eaton RH, Smith JK, Whitby LG. Association of inorganicpyrophosphatase activity with human alkaline-phosphatase preparations. Biochem J. 1967;102:53–57.

Murshed M, Harmey D, Milla´n JL, McKee MD, Karsenty G. Unique coexpression in osteoblasts of broadly expressed genes accounts for the spatial restriction of ECM mineralization to bone. Genes Dev. 2005;19:1093–1104.

Narisawa S, Fro¨ hlander N, Milla´n JL. Inactivation of two mouse alkaline phosphatase genes and establishment of a model of infantile hypophosphatasia. Dev Dyn. 1997;208:432–446.

Nielsen LB, Pedersen FS, Pedersen L. Expression of type III sodium-dependent phosphate transporters/ retroviral receptors mRNAs during osteoblast differentiation. Bone. 2001;28(2):160-6.

Palmer G, Zhao J, Bonjour J, Hofstetter W, Caverzasio J 1999 In vivo expression of transcripts encoding the Glvr-1 phosphate transporter/retrovirus receptor during bone development. Bone 24:1–7

Palmer G, Guicheux J, Bonjour JP, Caverzasio J 2000 Transforming growth factor-beta stimulates inorganic phosphate transport and expression of the type III phosphate transporter Glvr-1 in chondrogenic ATDC5 cells. Endocrinology 141:2236–2243.

Polewski MD, Johnson KA, Foster M, Millán JL, Terkeltaub R. Inorganic pyrophosphatase induces type I collagen in osteoblasts. Bone. 2010;46(1):81-90. PMCID: 2818162.

Roberts S., Narisawa S., Harmey D., Millán J.L., Farquharson C. Functional involvement of PHOSPHO1 in matrix vesicle-mediated skeletal mineralization. J. Bone Miner. Res. 2007;22(4):617-627.

Yadav MC, Simao AMS, Narisawa S, Huesa C, McKee MD, Farquharson C, Millán, JL. Loss of skeletal mineralization by the simultaneous ablation of PHOSPHO1 and alkaline phosphatase function: a unified model of the mechanisms of initiation of skeletal calcification. J Bone Miner Res. 2011;26:286-97.

Yoshiko Y, Candeliere GA, Maeda N, Aubin JE. Osteoblast autonomous Pi regulation via Pit1 plays a role in bone mineralization. Mol Cell Biol. 2007;27(12):4465-74. PMCID: 1900051.

Figure1.

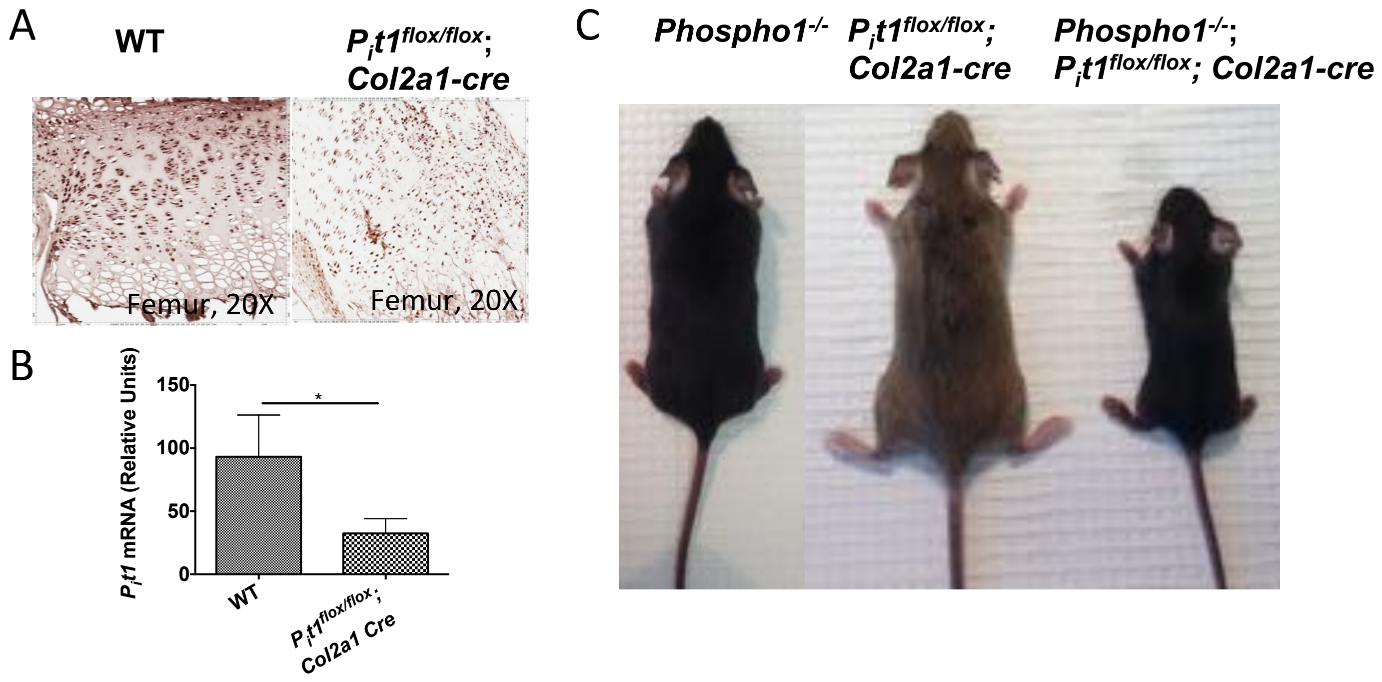
A
WT
$P_it1^{flox/flox}$; Col2a1-cre
Femur, 20X
Femur, 20X
B
150
100
50
0
P_it1 mRNA (Relative Units)
*
WT
$P_it1^{flox/flox}$; Col2a1 Cre
C
$Phospho1^{-/-}$
$P_it1^{flox/flox}$; Col2a1-cre
$Phospho1^{-/-}$; $P_it1^{flox/flox}$; Col2a1-cre

Figure 2

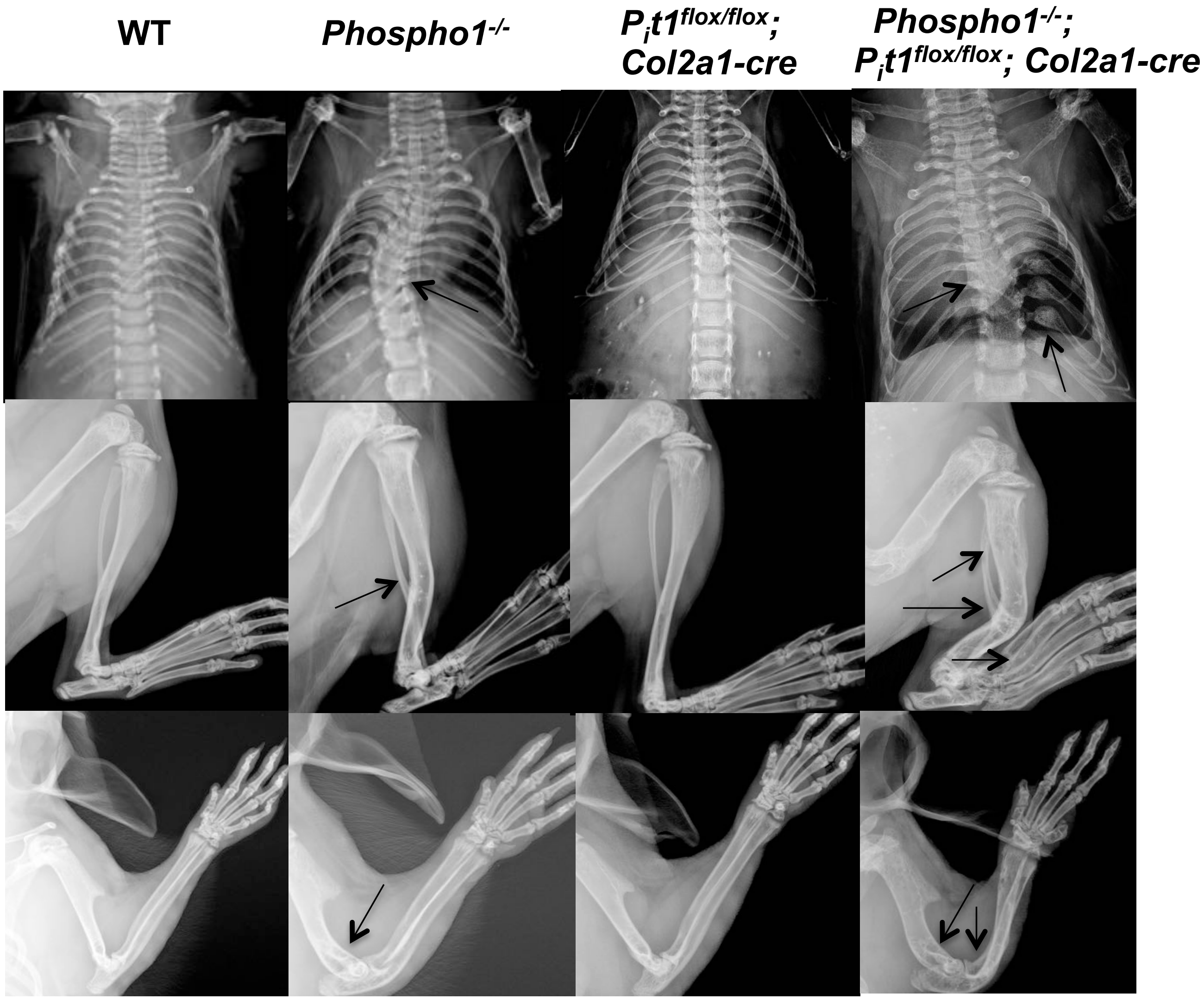
WT
Phospho1$^{-/-}$
P$_i$*t1*$^{flox/flox}$; *Col2a1-cre*
Phospho1$^{-/-}$; *P*$_i$*t1*$^{flox/flox}$; *Col2a1-cre*

Figure 3

A

Von Kossa-Van Gieson

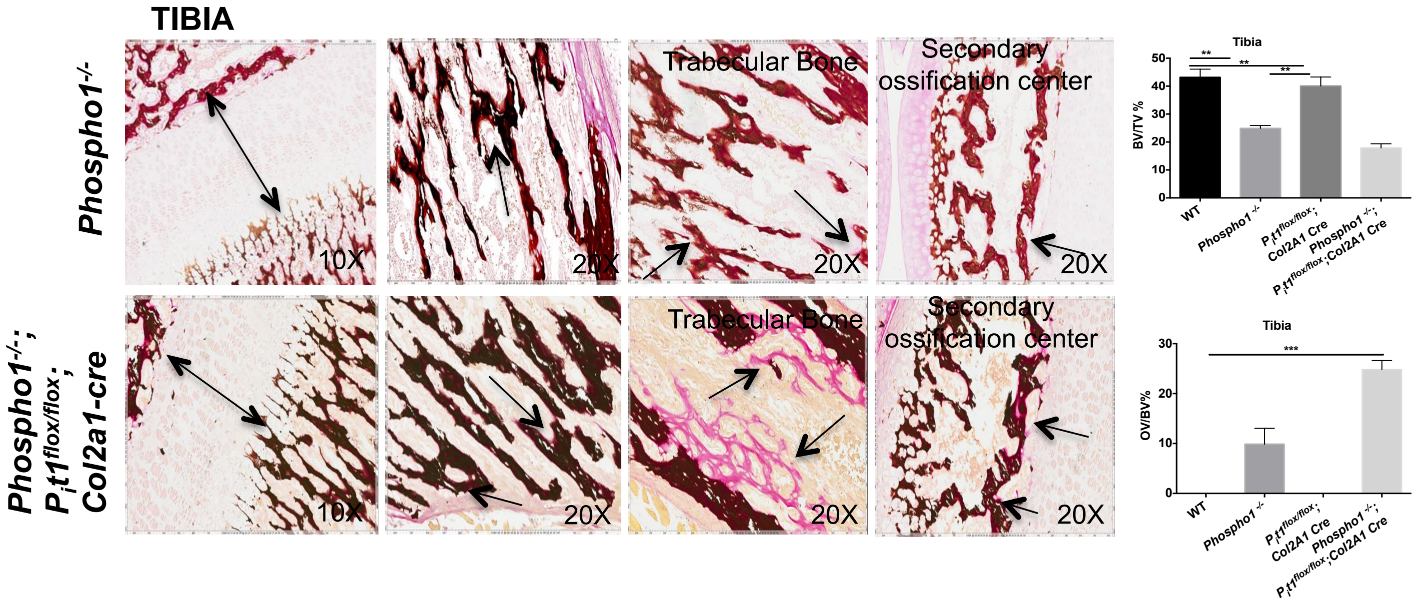

B

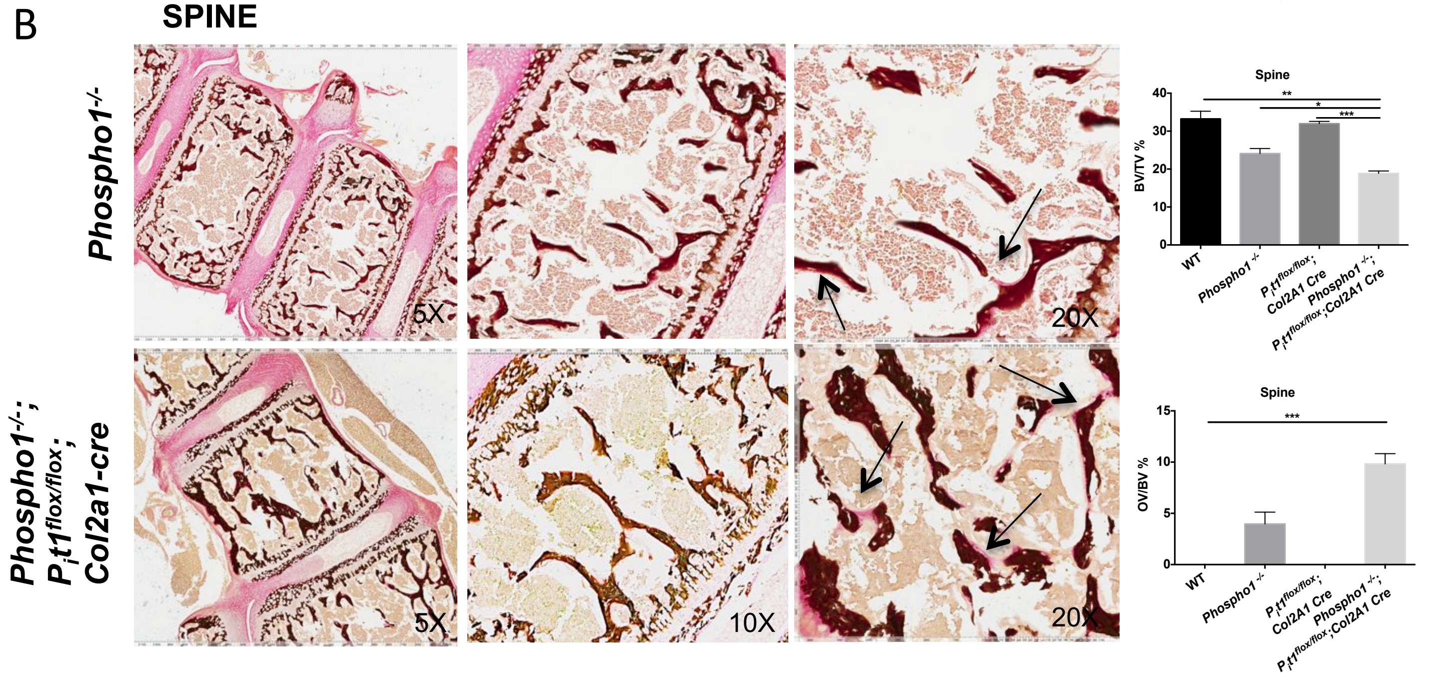

Figure 4

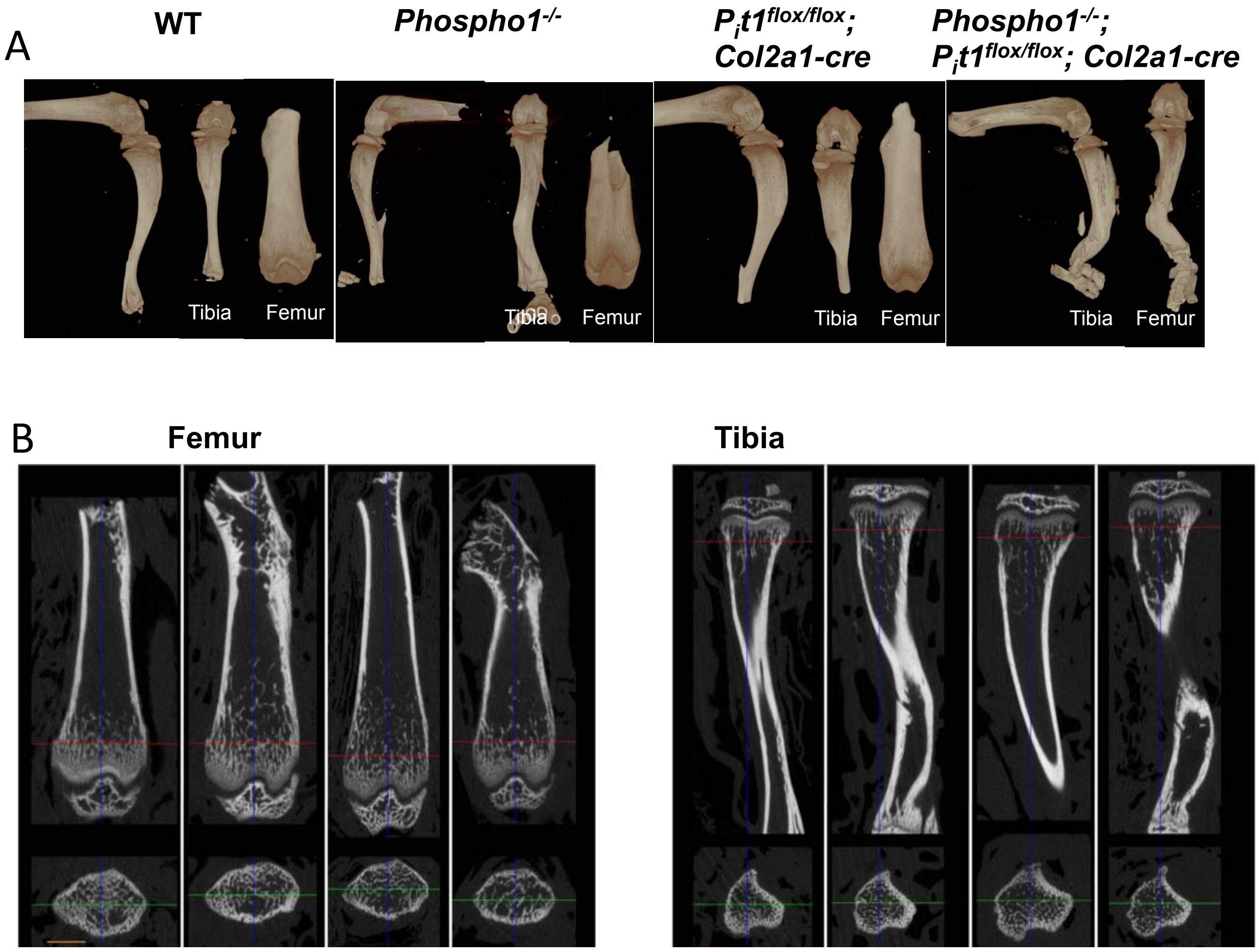
A
WT
Phospho1$^{-/-}$
P$_i$t1$^{flox/flox}$*; Col2a1-cre*
Phospho1$^{-/-}$*;*
P$_i$t1$^{flox/flox}$*; Col2a1-cre*
Tibia
Femur
Tibia
Femur
Tibia
Femur
Tibia
Femur
B
Femur
Tibia

Figure 5

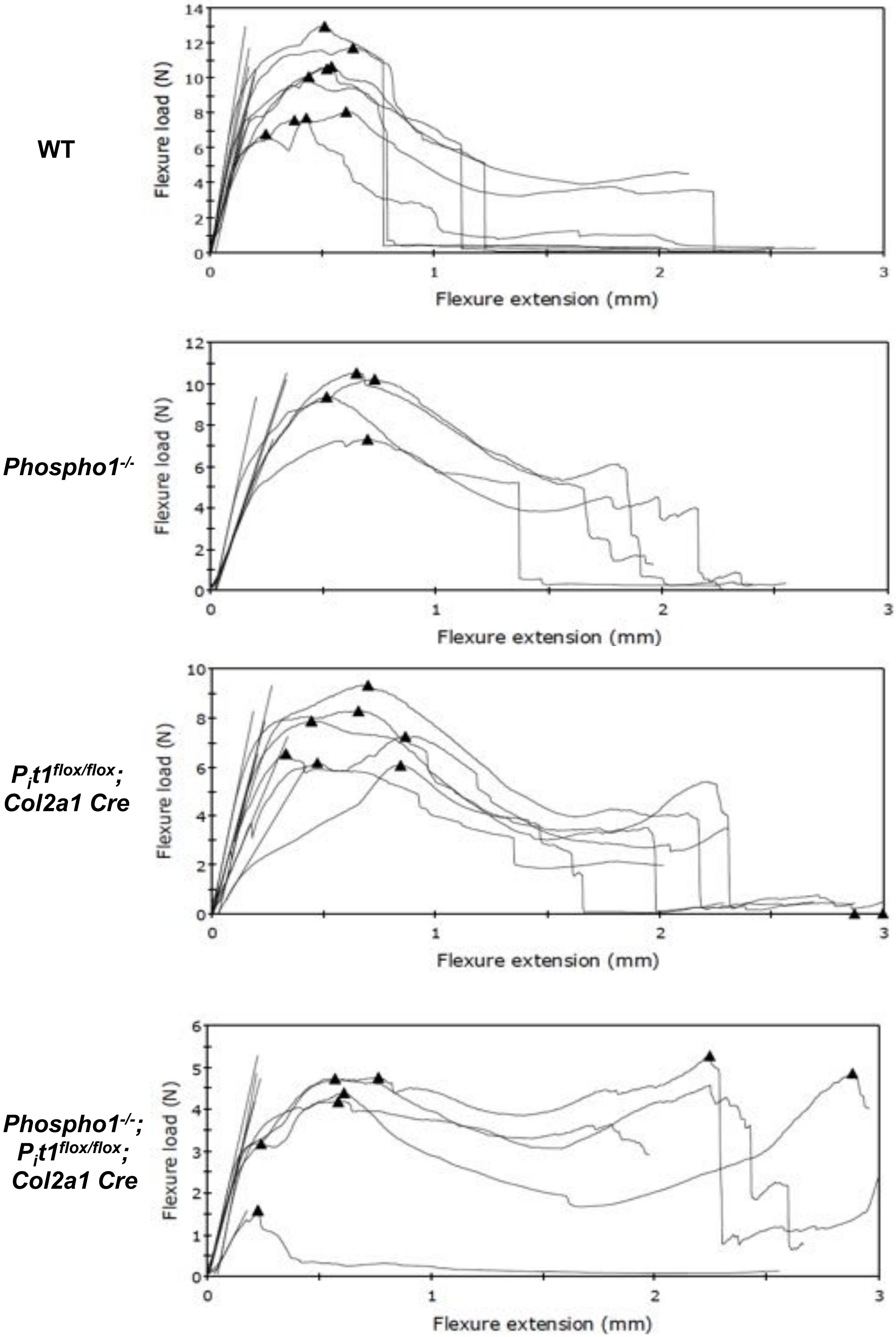
WT
Flexure load (N)
14
12
10
8
6
4
2
0
Flexure extension (mm)
0
1
2
3
Phospho1$^{-/-}$
Flexure load (N)
12
10
8
6
4
2
0
Flexure extension (mm)
0
1
2
3
P$_i$t1$^{flox/flox}$;
Col2a1 Cre
Flexure load (N)
10
8
6
4
2
0
Flexure extension (mm)
0
1
2
3
Phospho1$^{-/-}$;
P$_i$t1$^{flox/flox}$;
Col2a1 Cre
Flexure load (N)
6
5
4
3
2
1
0
Flexure extension (mm)
0
1
2
3

Figure 6

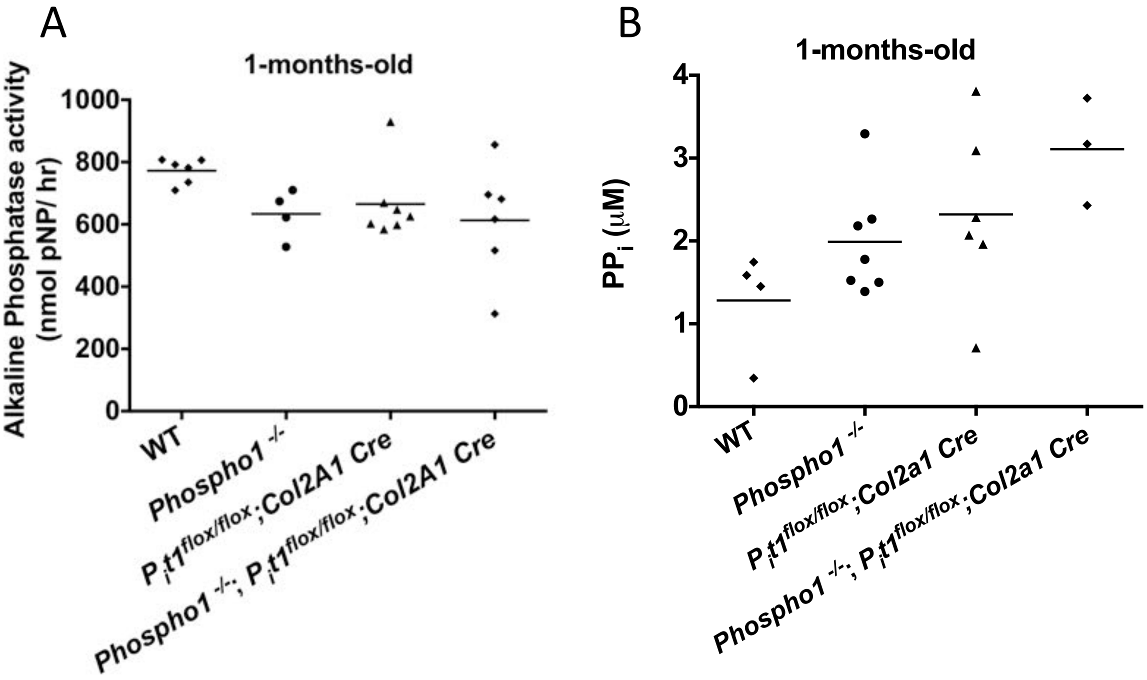
A
1-months-old
Alkaline Phosphatase activity (nmol pNP/ hr)
1000
800
600
400
200
0
WT
Phospho1 -/-
Pit1flox/flox;Col2A1 Cre
Phospho1 -/-; Pit1flox/flox;Col2A1 Cre
B
1-months-old
PPi (μM)
4
3
2
1
0
WT
Phospho1 -/-
Pit1flox/flox;Col2a1 Cre
Phospho1 -/-; Pit1flox/flox;Col2a1 Cre

Figure 7

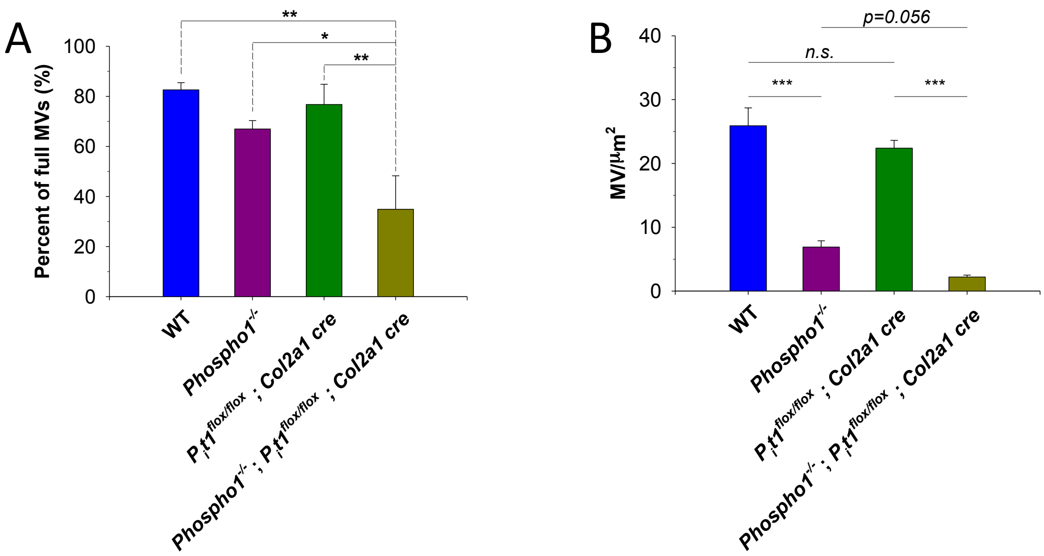
A
Percent of full MVs (%)
0
20
40
60
80
100
**
*
**
WT
Phospho1-/-
Pit1flox/flox ; Col2a1 cre
Phospho1-/- ; Pit1flox/flox ; Col2a1 cre
B
MV/μm2
0
10
20
30
40
p=0.056
n.s.
***
***
WT
Phospho1-/-
Pit1flox/flox ; Col2a1 cre
Phospho1-/- ; Pit1flox/flox ; Col2a1 cre

Supplemental Figure 1

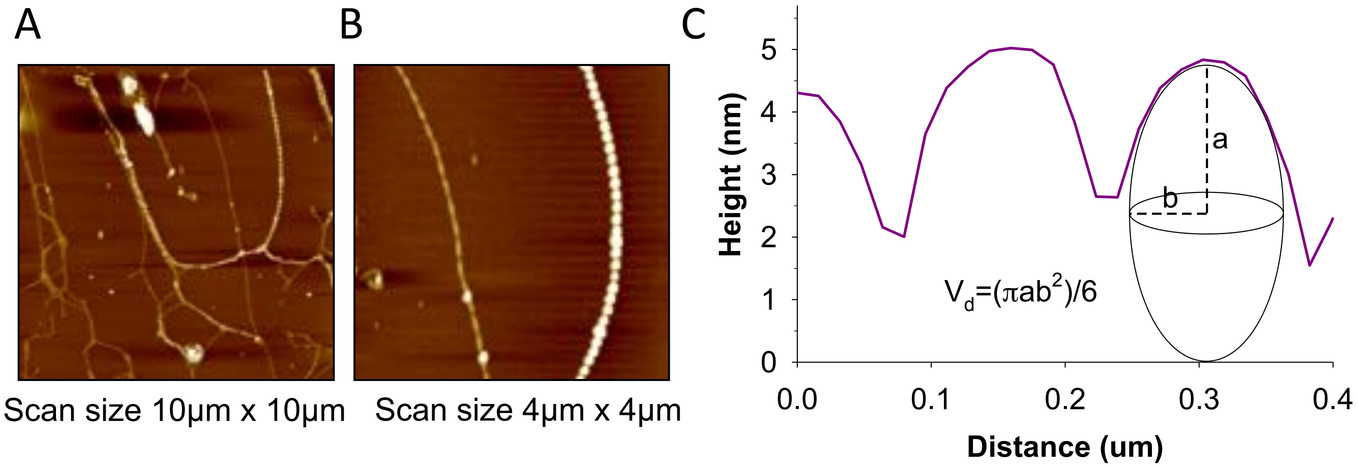

Scan size 10μm x 10μm

Scan size 4μm x 4μm

Supplemental Figure 2